Journal Pre-proof

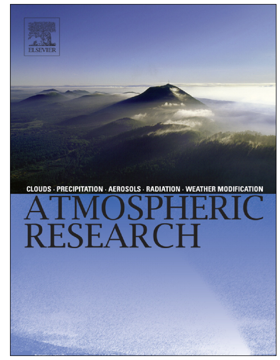

Impacts of the stochastic multicloud parameterization on the simulation of Western North Pacific summer rainfall

Libin Ma, Shuangyan Yang

PII: S0169-8095(19)31356-0

DOI: https://doi.org/10.1016/j.atmosres.2020.105067

Reference: ATMOS 105067

To appear in: *Atmospheric Research*

Received date: 20 October 2019

Revised date: 3 March 2020

Accepted date: 21 May 2020

Impacts of the Stochastic Multicloud Parameterization on the Simulation of Western North Pacific Summer Rainfall

Libin Ma[1] and Shuangyan Yang[2]

1. State Key Laboratory of Severe Weather, Chinese Academy of Meteorological Sciences, Beijing 100081, China

2. Key Laboratory of Meteorological Disaster, Ministry of Education (KLME)/Joint International Research Laboratory of Climate and Environmental Change (ILCEC)/Collaborative Innovation Center on Forecast and Evaluation of Meteorological Disasters (CIC-FEMD), Nanjing University of Information Science and Technology, Nanjing 210044, China

Submitted to *Atmospheric Research* on Oct. 20, 2019

Corresponding author: Libin Ma, Chinese Academy of Meteorological Sciences, South Zhongguancun Street No. 46, Beijing 100081, China

E-mail: malibin109@163.com

Corresponding author: Shuangyang Yang, Nanjing University of Information Science and Technology, Ningliu Road 219, Meteorology Bldg, Jiangsu, Nanjing 210044, China

E-mail: yangsy@nuist.edu.cn

Abstract

This study investigated the sensitivity of the western North Pacific (WNP) summer precipitation to the convection schemes and discussed the associated dynamical processes. Two convection schemes were compared: one is the default mass-flux convection scheme used in the state-of-the-art ECHAM6.3 atmosphere model and the other incorporates the Stochastic Multicloud Model (SMCM) into ECHAM6.3. Incorporation of the SMCM reduces the bias of cloud cover and shortwave and longwave radiation by regulating the shortwave and longwave cloud radiative forcing over the WNP. Compared to the default model, the modified model with the SMCM alleviates the dry bias in the WNP, which is associated with enhanced ascending motion. The moist static energy balance revealed that improved simulation of precipitation in the modified model is contributed by enhanced horizontal advection of moist enthalpy and increased net energy input the atmosphere, which is attributed to increased total cloud cover, over the WNP. Additionally, intensified latent energy advection over the WNP dominates enhanced horizontal advection of moist enthalpy in the modified model. On the other hand, the moisture budget analysis of the WNP demonstrated that strengthened convergence of moisture flux in the modified model plays the most influential role in reducing precipitation bias. Further analysis unraveled that enhanced zonal-mean moisture transported by the stationary eddy zonal flow convergence in the WNP dominates intensified zonal moisture convergence, thus increased horizontal convergence of moist flux in the modified model.

Keywords: the western North Pacific precipitation, the Stochastic Multicloud Model, ECHAM6.3 atmosphere model, Moist static energy balance, Moisture budget analysis

1. Introduction

It has long been known that the western North Pacific (WNP) is a key region to the anomalous summer weather in the East Asia and the global circulation (e.g., Nitta, 1987; Kawamura et al., 1999; Li and Wang, 2005; Qian and Shi, 2017). For example, since great latent heat releases to the upper troposphere over the WNP in summer time, the WNP acts as a peculiar monsoon region (Yanai and Tomita, 1998). The western North Pacific Subtropical High modulated by the convective activities occurred in WNP plays a vital role in propagating the moisture transport from the western tropical Pacific to the East Asia (e.g., Zhu and Yang, 2003; Huang et al., 2004, 2007; Zhou and Yu, 2005; Yang and Zhu, 2008). Moreover, the atmosphere-ocean interaction in the tropical WNP and upper-level circulation anomaly over the WNP are considered to play important roles in linking the East-Asian climate to the El Niño-Southern Oscillation (ENSO) (Rasmusson and Arkin, 1987; Kawamura et al., 1999, 2001; Wang et al., 2000). Besides, WNP also acts as a confluence region, which combines the forcing from eastern Pacific and Indian Ocean to impact the East Asian Summer monsoon (Wang et al., 1999, 2000; Wu et al., 2009). Yun et al. (2010) investigated the combined effects of eastern Pacific and Indian Ocean warming on the July-August East Asian climate. Their results illustrated that a strong Pacific-Japan-like pattern induced by the eastern Pacific warming during July and a Eurasian-like wave pattern caused by the Indian Ocean warming during August were modulated by different mean thermal states. Moreover, the WNP summer monsoon considerably influences the tropical cyclonic activities (Wu et al., 2012; Choi et al., 2015). Therefore, well simulated summer climate, says precipitation and circulation, over the WNP is of crucial importance and helps us understand the regional weather and climate variability well.

Convective schemes exert tremendous influence on the model results such as the Asian summer monsoon (ASM) (Wu et al., 2007a, b; Chen et al., 2010; Yu et al., 2011; Ma et al., 2019b). However, current generation of convective schemes cannot completely resolve the cloud physics, especially in the horizontally low-resolution atmospheric general circulation models (AGCMs) and climate system models. To well represent the unresolved cloud physics, cloud-resolving model, which takes place of the AGCMs, is proposed (see Guichard and Couvreux 2017 for a review). Additionally, the superparameterization, which applies a two-dimensional could-resolving model, is embedded in AGCMs to represent the convective processes (Grabowski, 2001; Khairoutdinov and Randall, 2001). The cloud-resolving model and superparameterization are used to study the climatology and intraseasonal variability of the ASM (e.g., DeMott et al., 2013; Jin and Stan, 2016). Besides the benefits, however, integrations of models with superparametrization and cloud-resolving model are computationally expensive. Thus, an alternative method –the Stochastic Multicloud Model (SMCM)– is proposed (Khouider and Majda, 2006a, b; Khouider et al., 2010). It has been validated that incorporation of the SMCM into AGCMs and climate system models improves the simulation of the Madden-Julian Oscillation (Deng et al., 2015; Goswami et al., 2017; Peters et al., 2017; Ma et al., 2019a) and the climatology of East Asian summer monsoon (Ma et al., 2019b).

Given the background fields, the SMCM predicts the area fraction of each cloud type (congestus, deep, and stratiform clouds) per grid box using the Markov chain Monte Carlo method (Khouider et al., 2010). Different from conventional calculation of the transition rate between different cloud types, which is formulated in terms of power function, a *tanh*-function (Peters et al., 2017) is used in this study. The *tanh*-function has the ability to model the observed convective behavior (Peters et al., 2013). Provided by the vertical pressure velocity and specific humidity at 500 hPa, the SMCM predicts the area fraction of deep convection, which is used to adjust the base mass flux of deep convective cloud, in this study. Once the convection is invoked and the area fraction of deep convection is greater than zero, deep convection is performed and predicted area fraction of deep convection is used to calculate the bass mass flux of deep convective cloud. Otherwise, if the convection is diagnosed and predicted area fraction of deep convection equals to zero, shallow convection is performed.

It was pointed out that an implementation of the SMCM into AGCMs, i.e., ECHAM6.3 (Stevens et al., 2013), improves the simulation of precipitation in the WNP (7º–22ºN, 110º–150ºE) (Ma et al., 2019b,c). Although improvement of the simulated precipitation over WNP region is mentioned in those studies, it was only evaluated by the pattern correlation coefficient (PCC) and the normalized root-mean square error (NRMES) scores (Ma et al., 2019b) and the area-averaged seasonal variation including the PCC and NMRSE scores (Ma et al., 2019c). Following the preceding works, the current study aims to explore the dynamic processes, which are responsible for the improvement in simulating the WNP precipitation by applying the SMCM to ECHAM6.3, through discussing the moist static energy balance, the moisture budget analysis, and the decomposition of associated dominated term. Note that Ma et al. (2019b) only qualitatively discussed the impacts of SMCM on the EASM without discussions by using the moist static energy balance and the moisture budget analysis, which are used in this study. Moreover, no applications of the moist static energy balance and associated decomposition of the dominated term were discussed in Ma et al. (2019c). The rest of this study is arranged as follows. Section 2 introduces the model, data, and corresponding methodologies. The results in view of moist static energy balance analysis are discussed in Sect. 3, following the moisture budget analysis in Sect. 4. Finally, Sect. 5 includes the conclusions and discussion.

2. Model, data and methods

2.1 Model description

The model used in this study is ECHAM6.3.02, which is one of subversions of the family of ECHAM6.3 and is used as the atmospheric component of Nanjing University of Information Science and Technology Earth System Model version 3 (NESM3) (Cao et al., 2018). Readers can refer to Stevens et al. (2013) and Mauritsen et al. (2019) for details. For simplicity, the model used in this study is referred to as ECHAM6.3.

The default convection scheme implemented in ECHAM6.3 is the mass-flux scheme of Tiedtke (1989) with modifications for penetrative convection (Nordeng, 1994). The mass-flux scheme includes organized entrainments and detrainments. It is assumed that organized entrainment occurs and makes the air flow enter into the cloud when the buoyance is positive, while the organized detrainment takes place when the buoyance is negative. Given the fractional entrainment rate ϵ_i for an individual updraft i, the organized entrainments (E) for the cloud ensemble, respectively, have the following form:

$$E = \sum_i M_i \epsilon_i = \sum_i \bar{\rho} \sigma_i w_i \epsilon_i, \tag{2.1}$$

where M_i, $\bar{\rho}$, σ_i, and w_i are the cloud-base mass flux, air density at cloud base, fractional area, and vertical velocity of the updraft i, respectively. For example, the mass flux at cloud bass M_d for deep convection equals to $M_d = \bar{\rho}\sigma_d w_d$.

During the implementation of the SMCM into ECHAM6.3, the SMCM is considered as a tool to predict the area fraction of deep convection σ_d^s, which is the candidate used to calculated the M_d. With combination of the default convection scheme, if the deep convection is invoked and the predicted σ_d^s by the SMCM is larger than zero, then M_d is adjusted by σ_d^s and $M_d = \bar{\rho}\sigma_d^s w_d$. On the other hand, if σ_d^s equals to zero, then the shallow convection is enforced. Details of the model description and implementation of SMCM into ECHAM6.3 can be referred to Peter et al. (2017) and Ma et al. (2019a, b).

2.2 Data

Two sets of AMIP-type experiments are conducted in this study. One is implemented with the default settings; the other couples the SMCM. The two experiments are referred to as ECHAM_CTRL and ECHAM_SMCM, respectively. Each set has ten members and the ensemble mean is used in order to eliminate the noise. The T63L47, which has 1.9º × 1.9º and 47 levels extending from the surface to the 0.01hPa in the horizontal and vertical directions, respectively, was configured in this study. In addition, each AMIP-type experiment runs from 1976 to 2014, with the boundary data and external forcing from the Coupled Model Intercomparison Project phase 6. The first three years are taken as the spinup phase and the last 36-year data are used for analysis.

Monthly data, including the winds, air temperature, precipitation, evaporation, specific humidity, and cloud cover from the ERA-Interim (Dee et al., 2011), are referred to as observation for comparison. Moreover, a combined monthly precipitation data, which is the arithmetic mean of GPCP (Adler et al., 2003) and CMAP (Xie and Arkin, 1997), following Wang et al. (2014) and Li et al. (2018), is also used. All monthly datasets spanning from 1979 to 2014, including model results, are horizontally interpolated onto 2.5º × 2.5º with bilinear-interpolation approach. Additionally, the monthly climatology of shortwave and longwave radiative fluxes and cloud radiative forcing from CERES-EBAF (Clouds and Earth's Radiant Energy System – Energy Balanced and Filled) (Loeb et al., 2009) are also used in this study.

2.3 Methods

It has been found that the moist static energy balance analysis is an effective approach to quantify the dominant term contributing to the distribution of precipitation in the monsoon regions (Chou and Neelin, 2003; Chen and Bordoni, 2014; Yao et al., 2017). Under the condition of the quasi-equilibrium state of vertical convection, the vertical mass integral of moist static energy balance averaged over a climatological period can be expressed as follows:

$$\overline{\langle\frac{\partial M}{\partial t}\rangle} = \overline{F_{net}} - \overline{\langle\vec{V}\cdot\nabla M\rangle} - \overline{\langle\omega\frac{\partial h}{\partial p}\rangle} \quad (2.2)$$

Where $\overline{F_{net}}$ can be written as:

$$\overline{F_{net}} = S_t^{\downarrow} - S_t^{\uparrow} - S_s^{\downarrow} + S_s^{\uparrow} - R_t^{\uparrow} + R_s^{\uparrow} - R_s^{\downarrow} + SH + LH \quad (2.3)$$

where $M = c_pT + l_vq$ and $h = c_pT + l_vq + gz$ are the moist enthalpy and moist static energy, respectively, with T is the air temperature, q is specific humidity, and z geopotential height; c_p and l_v are the specific heat at constant pressure and the latent heat of vaporization, respectively. $\overline{F_{net}}$ is the net energy flux into the atmosphere with which the subscripts s and t represent the surface and the top of atmosphere, respectively. $\vec{V}$ is the horizontal wind vector and ω is the vertical pressure velocity. $\langle X\rangle$ denotes the vertical mass integral and $\bar{X}$ is the temporal mean of the June-July-August-September (JJAS) season.

Additionally, the net precipitation distribution in the WNP rainfall band needs to satisfy the following moisture budget analysis (Chou and Lan, 2012):

$$\bar{P} = \bar{E} - \overline{\langle\partial_t q\rangle} - \overline{\langle\nabla\cdot(\vec{V}q)\rangle} - \overline{\langle\partial_p\omega q\rangle} \quad (2.4)$$

where P and E are the precipitation and evaporation, respectively. Note that the tendency term $-\overline{\langle\partial_t q\rangle}$ can be ignored when it is averaged over a climatological period.

Each of dependent variables may be decomposed into three components, a temporal mean, a stationary, and a transient eddies component, which are represented by overbar, star, and prime, respectively. Conventionally, $(\cdot)'$ represents the deviation from the JJAS-mean for each individual year and $(\cdot)^*$ denotes the deviation from the global zonal mean (e.g., Chen and Bordoni, 2014; Sun et al., 2016; Yao et al., 2017). Consequently, we have

$$\overline{\langle \vec{V} \cdot \nabla X \rangle} \approx \langle [\bar{\vec{V}}] \cdot [\nabla \bar{X}] \rangle + \langle [\bar{\vec{V}}] \cdot \nabla \bar{X^*} \rangle + \langle \bar{\vec{V^*}} \cdot [\nabla \bar{X}] \rangle + \langle \bar{\vec{V^*}} \cdot \nabla \bar{X^*} \rangle + \langle \bar{\vec{V'}} \cdot \nabla \bar{X'} \rangle \quad (2.5)$$

where X can be the moist enthalpy M or other variables.

3. Model results

3.1 Heat fluxes response to convective schemes

Combined with the default convective scheme, the SMCM adjusts the convective activities during its implementation in the atmosphere model, which definitely affects the distribution of cloud. Figure 1 shows the distributions of low-level, middle-level, and high-level cloud cover among observation and model simulations in JJAS. Observationally, more cloud appears in the high level, especially over the tropical regions, whilst less cloud appears in the low and middle levels (Figs. 1a-1c). Compared to the observation, the low and middle cloud cover in ECHAM_CTRL is underestimated and overestimated over the tropical and subtropical regions, respectively (Figs. 1d-1e). Disparate distribution is found in the high-level cloud cover. The cloud is obviously underestimated in the WNP and is overestimated in other regions compared to the observation (Fig. 1f). The biases of cloud cover lead to the drift of the radiation allowing more solar radiation into the atmosphere and more shortwave radiation reaches the earth surface compared to the observation. In addition, the less cloud cover also suggests that less heat energy is stored over the WNP. The bias of cloud cover in ECHAM_SMCM is disparately simulated compared to ECHAM_CTRL. Regarding the low-level cloud cover, the negative bias is reduced over the South China Sea and tropical North Pacific in ECHAM_SMCM, whereas the low-level cloud cover is overestimated over the subtropical North Pacific (Fig. 1g). Different from the negative bias modeled in ECHAM_CTRL, the positive bias appears over the WNP in ECHAM_SMCM (Fig. 1h). Although the high-level cloud cover is still underestimated over the WNP in EHCAM_SMCM, the bias is largely reduced compared to ECHAM_CTRL (Fig. 1i). The bias distribution indicates that more cloud cover is simulated in ECHAM_SMCM, implying that more heat energy is stored in the atmosphere compared to ECHAM_CTRL.

Changes in cloud cover no doubt exert influences on the energy balance (e.g., Zhou et al., 2015). How does the modification of cloud cover in ECHAM_SMCM affect the energy budget? Figure 2 depicts the top-of-the-atmosphere (TOA) shortwave, longwave, and net cloud radiative forcing among observation and model simulations in JJAS. Observationally, the net cloud radiative forcing is dominated by the shortwave radiative cloud forcing (Figs. 2a, 2d, and 2g). Compared to the contribution of shortwave cloud radiative forcing, for example, magnitude of the longwave cloud radiative forcing over the WNP is about 10 W m^{-2}, which is much smaller than that of the shortwave cloud radiative forcing with 100 W m^{-2} regardless the direction. Similar results are obtained in model simulations. Compared to the observation, the shortwave cloud radiative forcing is underestimated in ECHAM_CTRL over the WNP (Fig. 2b), whilst the longwave cloud radiative forcing is comparable between ECHAM_CTRL and the observation (Fig. 2e). Analogous results are reached in ECHAM_SMCM but with smaller bias in the shortwave cloud radiative forcing, especially over the WNP (Fig. 2c), which leads to the bias of net cloud radiative forcing over the WNP in ECHAM_SMCM is smaller compared to ECHAM_CTRL (Figs. 2h and 2i).

Figure 3 shows the TOA solar radiation and outgoing longwave radiation (OLR) in JJAS. Observationally, the solar radiation and OLR have similar distributions over the ocean, with the property that the magnitudes over the WNP are smaller than those over the subtropical North Pacific (Figs. 3a and 3d). The difference among the observation and model simulations illustrates that the observed features of the JJAS solar radiation and OLR at TOA are reproduced in ECHAM_CTRL and ECHAM_SMCM. In addition, similar bias patterns are found in model simulations but the smaller biases are found in ECHAM_SMCM compared to ECHAM_CTRL (Figs. 3b-3c and 3e-3f). Note that similar results are obtained with respect to the surface energy balance, including the cloud raidative forcing and shortwave and longwave radiations (figure not shown).

Aforementioned discussions indicate that implementation of the SMCM into the ECHAM6.3 reduces the bias of cloud cover and the radiative energy. This implies the heating over the tropics and extratropics would be redistributed, which further influences the atmospheric circulation (e.g., Trenberth et al., 2000), the organized tropical convection (e.g, Peters et al., 2013, 2017; Ma et al., 2019a), and the moist static energy (e.g., Webster, 1994). Moreover, incorporation of the stochastic convective forcing plays a vital role in influencing the monsoon and Hadley circulation (De La Chevrotiere and Khouider, 2016) and in improving the simulation of large-scale circulation of the East Asian summer monsoon (Ma et al., 2019b). Thus, to further explore impacts of the SMCM on the simulated precipitation in WNP in JJAS, the moist static energy balance and the moisture budget analysis are applied to investigate what controls the physical processes of the distribution of precipitation in the WNP in the following sections.

3.2 Climatology in summer

Figure 4 shows the JJAS-mean rainfall (shading) and 500-hPa vertical velocity (contour) during the period of 1979–2014. Observationally, as shown in Fig. 4a, heavy rainfall appears over the tropical WNP extending from the South China Sea to the open ocean west of 150°E. The 500-hPa vertical velocity over the WNP depicts the ascending motion, matching the spatial pattern of precipitation well. As shown in Fig. 4b, less rainfall and weaker ascending motion are found over the WNP in ECHAM_CTRL compared to the observation. The biases of precipitation and 500-hPa vertical velocity are reduced in ECHAM_SMCM (Fig. 4c). The area-averaged precipitation in ECHAM_SMCM (8.40 mm day^{-1}) is comparable to that in observation (8.43 mm day^{-1}) and is larger than that in ECHAM_CTRL (5.32 mm day^{-1}). In addition, the PCC of precipitation (500-hPa vertical velocity) in ECHAM_SMCM is 0.67 (0.84) versus -0.27 (-0.43) in ECHAM_CTRL, indicating that ECHAM_SMCM performs better in simulating the precipitation and vertical motion in the WNP region.

3.3 The moist static energy balance

To differentiate the relative contribution among humidity, air temperature, large-scale circulation, and radiation processes in simulating the WNP summer precipitation in ECHAM_SMCM, the moist static energy budget is diagnosed. Figure 5 shows the JJAS-mean net energy input into the atmosphere $\overline{F_{net}}$, the vertical–mass integrated horizontal advection of moist enthalpy $-\overline{\langle\vec{V}\cdot\nabla M\rangle}$, and the vertical MSE advection $-\overline{\langle\omega\frac{\partial h}{\partial p}\rangle}$. As shown in Fig. 5a, the observational $\overline{F_{net}}$ (the first row) is positive and negative in the tropical and subtropical WNP respectively. It indicates that the atmosphere gains net energy at tropics and losses net energy at subtropics, which establishes strong meridional gradient of air temperature between tropics and subtropics (Chen and Bordoni, 2014; Yao et al., 2017). Compared to the observation, $\overline{F_{net}}$ into the atmosphere is underestimated in ECHAM_CTRL over the WNP (the first row in Fig. 5b), implying a weakened meridional gradient of air temperature between tropics and subtropics. However, this bias is reduced in ECHAM_SMCM with the $\overline{F_{net}}$ is comparable to the observation over the WNP (the first row in Fig. 5c), generating stronger meridional gradient of air temperature than that in ECHAM_CTRL. The intensified meridional gradient of air temperature allows ECHAM_SMCM to perform better in simulating the onset of East Asian summer monsoon compared to ECHAM_CTRL (Ma et al., 2019b).

Model simulations display distinct spatial patterns of horizontal advection of moist enthalpy compared to the observation. Opposite to the negative observational horizontal moist enthalpy advection $-\overline{\langle \vec{V} \cdot \nabla M \rangle}$ which offsets the positive $\overline{F_{net}}$, the $-\overline{\langle \vec{V} \cdot \nabla M \rangle}$ is prevailing positive over the WNP in ECHAM_CTRL (the second row in Fig. 5a, b). Different $-\overline{\langle \vec{V} \cdot \nabla M \rangle}$ distribution appears over the WNP in ECHAM_SMCM compared to ECHAM_CTRL. As shown in Fig. 5c (the second row), the $-\overline{\langle \vec{V} \cdot \nabla M \rangle}$ in ECHAM_SMCM, in general, has the same sign as in the observation, but with smaller value over the open ocean in the WNP. In addition, the horizontal advection of moist enthalpy over southern China and eastern Vietnam is overestimated in ECHAM_SMCM compared to the observation.

The bottom panel in Fig. 5 shows the vertical moist static energy advection $-\overline{\langle \omega \frac{\partial h}{\partial p} \rangle}$ in the observation and model simulations. Note that the vertically integrated stratification of moist static energy $\overline{\langle \frac{\partial h}{\partial p} \rangle}$ in the troposphere is negative. Thus, negative $-\overline{\langle \omega \frac{\partial h}{\partial p} \rangle}$ over the WNP corresponds to the ascending motion. Observationally, as shown in the bottom panel in Fig. 5a, a convection center spans from the eastern South China Sea to the WNP, which is associated with the heavy rainfall depicted in Fig. 4a. Compared to the observation, the vertical convection of moist static energy is underestimated in ECHAM_CTRL and ECHAM_SMCM (bottom panels in Fig. 5b, c). However, compared to ECHAM_CTRL, the ascending motion of moist static energy is enhanced in EHCAM_SMCM, corresponding to an increase of precipitation over the WNP.

To make a quantitive comparison, the area-averaged quantities over the WNP are plotted in Fig. 6. It is shown that, compared to ECHAM_CTRL, $\overline{F_{net}}$, $-\overline{\langle \vec{V} \cdot \nabla M \rangle}$, and $-\overline{\langle\omega\frac{\partial h}{\partial p}\rangle}$ are intensified in ECHAM_SMCM. Note that, in addition, residual of the three terms in the right hand of equation (2.2) is not zero, indicating the moist static energy budget in equation (2.2) does not close in observation and model simulations. The disclosure of moist static energy budget arises from the unresolved subgrid-scale motions and insufficient vertical resolution in the ERA-Interim and models (Berrisford et al., 2011; Chen and Bordoni, 2014). Thus, the summation of $\overline{F_{net}}$ and $-\overline{\langle\vec{V}\cdot\nabla M\rangle}$ is used to represent the vertical convection of moist static energy aiming to close the moist static energy budget (figure omitted). We will focus on the changes in $\overline{F_{net}}$ and $-\overline{\langle\vec{V}\cdot\nabla M\rangle}$ instead of $-\overline{\langle\omega\frac{\partial h}{\partial p}\rangle}$ in the following discussion.

What is responsible for the variations of $\overline{F_{net}}$ between ECHAM_CTRL and ECHAM_SMCM? Recalling the implementation of SMCM in this study, it adjusts the shallow-deep-trigger based on the predicted deep-convection area fraction, which affects the distribution of cloud. Figure 7 shows the total cloud cover in observation and model simulations. Observationally, large cloud cover is found over the WNP, which inhibits the radiative energy reaching the earth surface and reflecting more radiative energy back into atmosphere through the top of the atmosphere (TOA) (Fig. 7a). As shown in Fig. 7b, compared to the observation, the cloud cover is obviously underestimated in ECHAM_CTRL, especially over the South China Sea, which is also clearly illustrated by the difference between the observation and ECHAM_CTRL (Fig. 7d). The reduction of cloud cover over the WNP allows more radiative energy to reach the earth surface and to escape out of the TOA, leading to less net energy is stored in the atmosphere (Fig. 5). The bias of cloud cover over the WNP is reduced in ECHAM_SMCM, being comparable to that in observation (Fig. 7c and 7e). The difference between ECHAM_SMCM and ECHAM_CTRL definitely demonstrates the increased cloud cover in ECHAM_SMCM (Fig. 7f). The increased cloud cover over the WNP makes ECHAM_SMCM keep more radiative energy in the atmosphere in this region.

The horizontal moist enthalpy advection $-\overline{\langle \vec{V} \cdot \nabla M \rangle}$ can be divided into the horizontal advections of dry enthalpy $-\overline{c_p \langle \vec{V} \cdot \nabla T \rangle}$ and of latent energy $-\overline{l_v \langle \vec{V} \cdot \nabla q \rangle}$ (Fig. 8). Unlike the case in the subtropical front where $-\overline{c_p \langle \vec{V} \cdot \nabla T \rangle}$ dominates $-\overline{\langle \vec{V} \cdot \nabla M \rangle}$ in the core of the Meiyu-Baiu front (Chen and Bordoni, 2014; Yao et al., 2017), the horizontal latent energy advection dominates $-\overline{\langle \vec{V} \cdot \nabla M \rangle}$ in JJAS over the WNP, indicating different dynamical processes in sustaining the precipitation between tropics and subtropics. As listed in Table 1, the area-averaged $-\overline{l_v \langle \vec{V} \cdot \nabla q \rangle}$ over the WNP in observation, ECHAM_CTRL, and ECHAM_SMCM is -11.77 W m^{-2}, -3.83 W m^{-2}, and -7.69 W m^{-2}, respectively. This indicates that the contribution of $-\overline{l_v \langle \vec{V} \cdot \nabla q \rangle}$ to the horizontal advection of moist enthalpy is enhanced in ECHAM_SMCM compared to ECHAM_CTRL.

To explore the physical processes contributing to $-\overline{l_v \langle \vec{V} \cdot \nabla q \rangle}$, following the method described in Sect. 2, $-\overline{l_v \langle \vec{V} \cdot \nabla q \rangle}$ is decomposed into five terms, the stationary eddy latent energy by the zonal-mean flow $-l_v \langle \left[\overline{\vec{V}}\right] \cdot \overline{\nabla q^*} \rangle$, the advection of the zonal-mean latent energy by stationary eddy velocity $-l_v \langle \overline{\vec{V^*}} \cdot [\overline{\nabla q}] \rangle$, the pure stationary eddy flux $-l_v \langle \overline{\vec{V^*}} \cdot \overline{\nabla q^*} \rangle$, the transient eddy flux $-l_v \langle \overline{\vec{V'} \cdot \nabla q'} \rangle$, and the zonal mean $-l_v\langle[\bar{\vec{V}}]\cdot\overline{[\nabla q]}\rangle$. Note that the $-l_v\langle[\bar{\vec{V}}]\cdot\overline{[\nabla q]}\rangle$ and $-l_v\langle\overline{\vec{V}'\cdot\nabla q'}\rangle$ are much smaller than other terms and can be neglected in the following discussion. Figure 9 displays other three terms of the observation and model simulations. Opposite to the contributions of the $-l_v\langle[\bar{\vec{V}}]\cdot\overline{\nabla q^*}\rangle$ and $-l_v\langle\overline{\vec{V}^*}\cdot\overline{\nabla q^*}\rangle$ (the first and third rows in Fig. 9), which have the same sign of $-\overline{l_v\langle\vec{V}\cdot\nabla q\rangle}$, $-l_v\langle\overline{\vec{V}^*}\cdot\overline{[\nabla q]}\rangle$ offsets the contributions of $-l_v\langle[\bar{\vec{V}}]\cdot\overline{\nabla q^*}\rangle$ and $-l_v\langle\overline{\vec{V}^*}\cdot\overline{\nabla q^*}\rangle$ in the WNP (the second row in Fig. 9). Compared to ECHAM_CTRL, in addition, it can be distinguished that the contributions of the $-l_v\langle[\bar{\vec{V}}]\cdot\overline{\nabla q^*}\rangle$, $-l_v\langle\overline{\vec{V}^*}\cdot\overline{[\nabla q]}\rangle$, and $-l_v\langle\overline{\vec{V}^*}\cdot\overline{\nabla q^*}\rangle$ are enhanced in ECHAM_SMCM, regardless of the positive or negative influence on changes in the $-\overline{l_v\langle\vec{V}\cdot\nabla q\rangle}$. To clearly clarify the enhanced contributions, area-weighted mean of each term over the WNP is summarized in Table 1. The contribution of $-l_v\langle[\bar{\vec{V}}]\cdot\overline{\nabla q^*}\rangle$ to $-\overline{l_v\langle\vec{V}\cdot\nabla q\rangle}$ in ECHAM_CTRL is only half of the observation, that is -7.43 W m^{-2} in ECHAM_CTRL versus -14.99 W m^{-2} in the observation. The bias is reduced in ECHAM_SMCM. The mean value of $-l_v\langle[\bar{\vec{V}}]\cdot\overline{\nabla q^*}\rangle$ in ECHAM_SMCM is -13.75 W m^{-2}. In addition, the mean value of $-l_v\langle\overline{\vec{V}^*}\cdot\overline{[\nabla q]}\rangle$ and $-l_v\langle\overline{\vec{V}^*}\cdot\overline{\nabla q^*}\rangle$ in ECHAM_CTRL (ECHAM_SMCM) are 12.64 (23.71) W m^{-2} and -10.36 (-18.60) W m^{-2}, respectively. Note that ECHAM_SMCM almost double the contribution of $-l_v\langle[\bar{\vec{V}}]\cdot\overline{\nabla q^*}\rangle$, $-l_v\langle\overline{\vec{V}^*}\cdot\overline{[\nabla q]}\rangle$ and $-l_v\langle\overline{\vec{V}^*}\cdot\overline{\nabla q^*}\rangle$ to $-\overline{l_v\langle\vec{V}\cdot\nabla q\rangle}$ compared to ECHAM_CTRL. Moreover, comparison of the area-averaged $-l_v\langle\overline{\vec{V}'\cdot\nabla q'}\rangle$ over the WNP among observation and model simulations shows that the negative contribution of $-l_v\langle\overline{\vec{V}'\cdot\nabla q'}\rangle$ to $-\overline{l_v\langle\vec{V}\cdot\nabla q\rangle}$ is also enhanced in ECHAM_SMCM compared to ECHAM_CTRL.

3.4 The moisture budget analysis

A moisture budget analysis is also applied to investigate the physical processes distributing net precipitation in the WNP. Observationally, strong moist flux convergence (shadings in Fig. 10a) and evaporation (contour in Fig. 10a) are found in the WNP, which is associated with heavy rainfall in this region (Fig. 4a). The moist-flux convergence suggests that the moisture is transported upward to sustain the precipitation in the WNP. As for model simulations, the moist-flux convergence and evaporation are underestimated in ECHAM_CTRL, especially in the South China Sea, compared to the observation (shadings in Fig. 10e). Simulations of the moist-flux convergence and evaporation are improved in ECHAM_SMCM, as shown in Fig. 10i, which are comparable to the observation. This possibly interprets why ECHAM_SMCM performs better in simulating precipitation in the WNP compared to ECHAM_CTRL. In addition, the distribution of net precipitation in the WNP is less contributed by the vertical convection of moist in observation and model simulations when compared to the moist-flux convergence and evaporation (Fig. 10b, 10f, and 10j). Moreover, the area-averaged value also validates that the observed and modeled net precipitation in the WNP is mainly attributed to the vertical integral of moist-flux convergence and local evaporation (Fig. 11).

The moist-flux convergence $-\overline{\langle \nabla \cdot \vec{V} q \rangle}$ can be reformulated as the summation of the zonal moisture convergence $-\overline{\langle \partial_x (uq) \rangle}$ and the meridional moisture convergence ($-\overline{\langle \partial_y (vq) \rangle}$) (Yao et al., 2017). As shown in Fig. 10 (the third and fourth rows), the zonal and meridional components of moist convergence generally play opposite roles in the distribution of $-\overline{\langle\nabla\cdot\vec{V}q\rangle}$. Regarding the zonal moisture convergence $-\overline{\langle\partial_x(uq)\rangle}$, it mainly contributes to the horizontal distribution of $-\overline{\langle\nabla\cdot\vec{V}q\rangle}$ (Fig. 10c, g, k); whereas, $-\overline{\langle\partial_y(vq)\rangle}$ offsets the contribution of $-\overline{\langle\partial_x(uq)\rangle}$ (Fig. 10d, h, l). The spatial pattern and area-averaged value indicate that the simulation of $-\overline{\langle\partial_x(uq)\rangle}$ is improved in ECHAM_SMCM compared to ECHAM_CTRL (third and fourth rows in Fig. 10 and Fig. 11).

Following the approach introduced in Sect. 2, the zonal moisture convergence ($-\overline{\langle\partial_x(uq)\rangle}$) can be further decomposed into corresponding mean, stationary, and transient terms. The stationary eddy terms include $-\langle\overline{u^*}\times\overline{\partial_x q^*}\rangle$, $-\langle\overline{[u]}\times\overline{\partial_x q^*}\rangle$, $-\langle\overline{[q]}\times\overline{\partial_x u^*}\rangle$, and $-\langle\overline{q^*}\times\overline{\partial_x u^*}\rangle$, which are associated with the zonal stationary eddy flow and zonal humidity distributions. On the other hand, the mean terms $-\langle\overline{[u]}\times\overline{\partial_x[q]}\rangle$ and $-\langle\overline{[q]}\times\overline{\partial_x[u]}\rangle$ related to the planetary-scale humidity and circulation are generally small and can be ignored. In addition, the transient eddy terms, $-\langle\overline{u'}\times\overline{\partial_x q'}\rangle$ and $-\langle\overline{q'}\times\overline{\partial_x u'}\rangle$, also play minor roles in determining the spatial pattern of $-\overline{\langle\partial_x(uq)\rangle}$ compared to the stationary eddy terms (Chen and Bordoni, 2014; Yao et al., 2017). Thus, only four stationary eddy terms are calculated and discussed in this study. The area-averaged values over the WNP are summarized in Table 2. Compared to ECHAM_CTRL, the zonal moisture convergence $-\overline{\langle\partial_x(uq)\rangle}$ is intensified in ECHAM_SMCM, which is comparable to observation. Except the product of stationary eddy flow and zonal gradient of stationary humidity ($-\langle\overline{u^*}\times\overline{\partial_x q^*}\rangle$), other three terms contribute to the improvement in simulating

$-\overline{\langle \partial_x (uq) \rangle}$. Of these terms, moreover, the zonal-mean moisture transported via the convergence of stationary eddy zonal flow ($-\langle \overline{[q]} \times \overline{\partial_x u^*} \rangle$) dominates the improvement, which is also the main factor in determining the spatial pattern of $-\overline{\langle \partial_x (uq) \rangle}$.

4. Conclusion and discussion

This study investigated the effects of the SMCM on the simulation of the WNP precipitation in JJAS. The corresponding physical processes responsible for the improvements is also diagnosed by applying the moist static energy balance and moisture budget analyses. The preliminary results are summarized as follows.

(1) In addition to the improvement in the simulation of precipitation revealed by Ma et al. (2019b,c), simulation of the JJAS ascending motion in the WNP is also improved in ECHAM_SMCM compared to ECHAM_CTRL with higher area-average value and PCC score.

(2) The moist static energy balance analysis revealed that the net energy into the atmosphere and horizontal advection of moist enthalpy sustain the rainfall over the WNP. The enhanced net energy into atmosphere and horizontal moist-enthalpy advection, compared to ECHAM_CTRL, lead to improvement in simulating distributions of the western North Pacific precipitation in ECHAM_SMCM. Further analyses indicated that increased total cloud cover over the WNP, which limits the radiative energy reaching the earth surface and decreases the refraction of radiative energy at the top of atmosphere, contributes to intensified net energy into the

atmosphere by coupling the SMCM into ECHAM6.3. In addition, intensification of the stationary eddy latent energy by the zonal-mean flow ($-l_v\langle\overline{[\vec{V}]\cdot\nabla q^*}\rangle$) and the pure stationary eddy flux ($-l_v\langle\overline{\vec{V^*}\cdot\nabla q^*}\rangle$) in ECHAM_SMCM dominates the improvements in simulating distributions of the horizontal advection of moist enthalpy.

(3) The moisture budget analysis of the western North Pacific demonstrated that improvement in simulating net precipitation in this region in ECHAM_SMCM mainly attributes to the intensified moist-flux convergence (-$\overline{\langle\nabla\cdot\vec{V}q\rangle}$), which is contributed by the zonal moisture convergence ($-\overline{\langle\partial_x(uq)\rangle}$). Decomposition analysis unraveled that the zonal-mean moisture transported via the convergence of stationary eddy zonal flow ($-\langle\overline{[q]\times\partial_x u^*}\rangle$) is the major factor to determine the distribution of $-\overline{\langle\partial_x(uq)\rangle}$.

Previous studies have addressed that the circulation over the WNP plays a vital role in linking the ENSO and East Asian climate (e.g., Wang et al., 2000). Although the simulation of precipitation and large-scale vertical convection over the WNP are improved in ECHAM_SMCM, whether the coupling of SMCM into the CSMs will improves the linkage between ENSO and East Asia climate is still unknown. The future work firstly couples the SMCM to a climate system model, i.e., the version three of Nanjing University of Information Science and Technology Earth System Model (NESM3) (Cao et al., 2018), then corresponding analyses are conducted to discuss the effects of the SMCM on the relationship between ENSO and East Asia climate through sensitive experiments.

Acknowledgements. The authors appreciate Prof. Bin Wang from University of Hawaii at Manoa for his constructive suggestions and Dr. Karsten Peters from Max-Planck-Institut für Meteorologie (now at Deutsches Klimarechenzentrum GmbH (DKRZ)) for his help on coupling the Stochastic Multicloud Model (SMCM) to the ECHAM6.3 atmosphere model. This work was supported by the National Key R&D Program of China (Grant No. 2018YFC1505803). This work was also sponsored by the Basic Research Fund of CAMS (2018Z007) and the Startup Foundation for Introducing Talent of NUIST (Grant No. 2018r027).

References

Adler R F, Huffman G J, Chang A, et al. 2003. The version-2 global precipitation climatology project (GPCP) monthly precipitation analysis (1979-present). J. Hydrometeorol., 4: 1147-1167.

Berrisford P, Kallberg P, Kobayashi S, et al. 2011. Atmospheric conservation properties in ERA-Interim. Q. J. R. Meteorol. Soc., 137: 1381-1399.

Cao J, Wang B, Yang Y-M, Ma LJ, et al. 2018. The NUIST Earth System Model (NESM) version 3: description and preliminary evaluation. Geosci. Model. Dev., 11:2975–2993.

Chen HM, Zhou TJ, Neale RB, et al. 2010. Performance of the new NCAR CAM3.5 in East Asian summer monsoon simulations: sensitivity to modifications of the convective scheme. J. Clim., 23: 3657-3675.

Chen J and Bordoni S. 2014. Orographic effects of the Tibetan Plateau on the East Asian summer monsoon: An energetic perspective. J. Clim., 27: 3052-3072.

Choi J-W, Kim B-J, Zhang BJ, et al. 2016. Possible relation of the western North Pacific monsoon to the tropical cyclone activity over western North Pacific. Int. J. Climatol., 36: 3334-3345.

Chou C and Neelin. 2003. Mechanisms limiting the northward extent of the northern summer monsoons over North America, Asia, and Africa. J. Clim., 16: 406-425.

Chou C and Lau C-W. 2012. Changes in the annual range of precipitation under global warming. J. Clim., 25: 222-235.

Dee DP, Uppala SM, Simmons AJ, et al. 2011. The ERA-Interim reanalysis: configuration and performance of the data assimilation system. Q. J. R. Meteorol. Soc., 137:553–597.

De La Chevrotiere M, Khouider B. 2016. A zonally symmetric model for the monsoon-Hadley circulation with stochastic convective forcing. Theor. Comput. Fluid Dyn., 31: 89-110.

DeMott C, Stan C, and Randall DA. 2013. Northward propagation mechanism of the Boreal Summer Intraseasonal Oscillation in the ERA-Interim and SP-CCSM. J. Clim., 26: 1973-1992.

Deng Q, Khouider B, and Majda AJ. 2015. The MJO in a coarse-resolution GCM with a stochastic multicloud parameterization. J. Atmos. Sci., 72:55–74.

Goswami BB, Khouider B, Phani R, Mukhopadhyay P, and Majda AJ. 2017. Improving synoptic and intraseasonal variability in CFSv2 via stochastic representation of organized convection. Geophy. Res. Lett., 44:1104–1113.

Grabowski WW. 2001. Coupling cloud processes with the large-scale dynamics using the cloud-resolving convection parameterization (CRCP). J. Atmos. Sci., 58: 978-997.

Guichard F and Couvreux F. 2017. A short review of numerical cloud-resolving models. Tellus, 69:1

Huang RH, Chen JL, and Huang G. 2007. Characteristics and variations of the East Asian monsoon system and its impacts on climate disasters in China. Adv. Atmos. Sci., 24: 993-1023.

Huang RH, Chen W, Yang B, Zhang R. 2004. Recent advances in studies of the interaction between the East Asian winter and summer monsoons and ENSO cycle. Adv. Atmos. Sci., 21: 407-424.

Jin Y and Stan C. 2016. Simulation of East Asian summer monsoon (EASM) in SP-CCSM4: Part I-Seasonal mean state and intraseasonal variability. J. Geophys. Res. Atmos., 121: 7801-7818.

Khairoutdinov MF and Randall DA. 2001. A cloud resolving model as a cloud parameterization in the NCAR community climate system model: preliminary results. Geophys. Res. Lett., 28: 3617-3620.

Khouider B, Biello J, and Majda AJ. 2010. A stochastic multicloud models for tropical convection. Commun. Math. Sci., 8:187-216.

Khouider B and Majda AJ. 2006a. Model multi-cloud parameterizations for convectively coupled waves: detailed nonlinear wave evolution. Dyn. Atmos. Oceans, 42:59-80.

Khouider B and Majda AJ. 2006b. A simple multicloud parameterization for convectively coupled tropical waves. Part I: linear analysis. J. Atmos. Sci., 63:1308-1323.

Kawamura R, Matsuura T, Ilizuka S. 2001. Interannual atmosphere-ocean variations in the tropical western North Pacific relevant to the Asian summer monsoon-ENSO coupling. 79: 883-898.

Kawamura R, Murakami T. 1998. Baiu near Japan and its relation to summer monsoons over southeast Asia and the western North Pacific. J. Meteor. Soc. Japan, 76: 619-639.

Li J, Yang Y-M, Wang B. 2018. Evaluation of NESMv3 and CMIP5 models' performance on simulation of Asian-Australian Monsoon. Atmosphere, 9, 327, doi:10.3390/atmos9090327.

Li T, Wang B. 2005. A review on the western North Pacific monsoon: synoptic-to-interannual variabilities. Terr. Atmos. Oceanic Sci., 16: 285-314.

Loeb NG, Wielicki BA, Doelling DR, et al. 2009. Toward optimal closure of the Earth's top-of-atmosphere radiation budget, J. Clim., 22: 748–766.

Ma LB, Peters K, Wang B, and Li J. 2019a. Revisiting the impact of Stochastic Multicloud Model on the MJO using low-resolution ECHAM6.3 atmosphere model. J. Meteor. Soc. Japan, 97: 977-993.

Ma LB, Zhu ZW, Li J and Cao J. 2019b. Improving the simulation of the climatology of the East Asian summer monsoon by coupling the Stochastic Multicloud Model to the ECHAM6.3 atmosphere model. Clim. Dyn., 53: 2061-2081.

Ma LB, Jiang ZJ, and Cao J. 2019c. Effects of a stochastic multicloud parameteriation on the simulated Asian-Australian monsoon rainfall in an AGCM. Inter. J. Climatol., doi:10.1002/joc.6352.

Nitta T. 1987. Convective activities in the tropical western Pacific and their impacts on the Northern Hemisphere summer circulation. J. Meteor. Soc. Japan, 65: 165-171.

Peters K, Crueger C, Jakob C, and Möbis B. 2017. Improved MJO-simulation in ECHAM6.3 by coupling a stochastic multicloud model to the convection scheme. J. Adv. Model. Earth Syst., 9:193–219.

Peters K, Jakob, Davies L, et al. 2013. Stochastic behavior of tropical convection in observations and a multicloud model. J. Atmos. Sci., 70: 3556-3575.

Qian WH, Shi J. 2017. Tripole precipitation and SST variations linked with extreme zonal activities of the western Pacific subtropical high. Int. J. Climatol., 37: 3018-3035.

Rasmusson EM and Arkin PA. 1987. El Niño/Southern Oscillation and the Asian monsoon. In: Yeh et al. (eds) The climate of China and global climate. China Ocean Press, Beijing, pp141-153.

Stevens B, Giorgetta M, Esch M, et al. 2013. Atmospheric component of the MPI-M earth system model: ECHAM6. J. Adv. Model. Earth Sys., 5:146–172.

Sun Y, Zhou TJ, et al. 2016. Drivers and mechanisms for enhanced summer monsoon precipitation over East Asia during the mid-Pliocene in the IPSL-CM5A. Clim. Dyn., 46: 1437-1457.

Trenberth K E, Stepaniak D P, Caron J M. 2000. The global monsoon as seen through the divergent atmospheric circulation. J. Clim., 13: 3969-3993.

Wang B, Wu RG, and Fu XH. 2000. Pacific-East Asian teleconnection: How does ENSO affect the East Asian climate? J. Clim., 13: 1517-1536.

Wang B, Wu RG, Lukas R. 1999. Roles of the western North Pacific wind variation in thermocline adjustment and ENSO phase transition. J. Meteor. Soc. Japan, 77:

1-16.

Wang B, Yim S-Y, Lee J-Y, Liu J, Ha K-J. 2014. Future change of Asian-Australian monsoon under RCP 4.5 anthropogenic warming scenario. Clim. Dyn., 42: 83-100.

Webster P J. 1994. The role of hydrographic processes in ocean-atmosphere interactions. Rev. Geophys., 32: 427-476.

Wu B, Zhou T J, Li T. 2009. Seasonally evolving dominant interannual variability modes of East Asian climate. J. Clim., 22: 2992-3005.

Wu L, Wen ZP, Huang RH, and Wu RG. 2012. Possible linkage between the monsoon trough variability and the tropical cyclone activity over the western North Pacific. Monthly Weather Review, 140: 140-150.

Wu X, Deng L, Song X et al. 2007a. Impact of a modified convective scheme on the Madden-Julian Oscillation and El Niño-Southern Oscillation in a coupled climate model. Geophys. Res. Lett., 34: L16823. doi: 10.1029/2007GL030637.

Wu X, Deng L, Song X et al. 2007b. Coupling of convective momentum transport with convective heating in global climate simulations. J. Atmos. Sci., 64: 1334-1349.

Xie P, Arkin P A. 1997. A 17-year monthly analysis based on gauge observations, satellite estimates, and numerical model outputs. Bull. Am. Meteorol. Soc., 78: 2539-2558.

Yanai M and Tomita T. 1998. Seasonal heating of the Tibetan Plateau and its effects on the evolution of the Asian summer monsoon. J. Meteor. Soc. Japan, 70: 319-351.

Yang XQ and Zhu YM. 2008. Interdecadal climate variability in China associated with the Pacific Decadal Oscillation. In: Fu C et al (eds) Regional climate studies of China. Springer, New York, pp97-118.

Yao JC, Zhou TJ, Guo Z, et al. 2017. Improved performance of high-resolution atmospheric models in simulating the East Asian summer monsoon rain belt. J. Clim., 30: 8825-8840.

Yu ET, Wang HJ, Gao YQ, and Sun JQ. 2011. Impacts of cumulus convective parameterization schemes on summer monsoon precipitation simulation over China. J. Meteor. Res., 25: 581-592.

Yun K-S, Ha K-J, Wang B. 2010. Impacts of tropical ocean warming on East Asian summer climate. Geophys. Res. Lett., 37, L20809, doi:10.1029/2010GL044931.

Zhou TJ, Yu RC. 2005. Atmospheric water vapor transport assosicated with typical anomalous summer rainfall patterns in China. J. Geophys. Res., 110, D08104, doi:10.1029/2004JD005413.

Zhu LJ, Bao Q, Liu YM, et al. 2015. Global energy and water balance: characteristics from finite-volume atmospheric model of the IAP/LASG (FAMIL 1). J. Adv. Model. Earth Syst., 7, 1-20, doi:10.1002/2014MS000349.

Zhu YM and Yang XQ. 2003. Relationships between Pacific Decadal Oscillation (PDO) and climate variabilities in China. Acta Meteor. Sinica, 64: 641-654.

Table and Figure Captions

Table 1 Area-weighted mean of $-l_v\langle\overline{\vec{V}\cdot\nabla q}\rangle$, $-l_v\langle\left[\bar{\vec{V}}\right]\cdot\overline{\nabla q^*}\rangle$, $-l_v\langle\overline{\vec{V}^*}\cdot\overline{[\nabla q]}\rangle$, $-l_v\langle\overline{\vec{V}^*}\cdot\overline{\nabla q^*}\rangle$, and $-l_v\langle\overline{\overrightarrow{V'}\cdot\nabla q'}\rangle$ in the WNP (unit in W m^{-2})

Table 2 Area-averaged value of $-\langle\overline{\partial_x(uq)}\rangle$, $-\langle\overline{u^*}\times\overline{\partial_x q^*}\rangle$, $-\langle\overline{[u]}\times\overline{\partial_x q^*}\rangle$, $-\langle\overline{[q]}\times\overline{\partial_x u^*}\rangle$, and $-\langle\overline{q^*}\times\overline{\partial_x u^*}\rangle$ in the WNP (unit in mm day^{-1})

Figure 1 JJAS-mean (a, d, g) low-level, (b, e, h) middle-level, and (c, f, i) high-level cloud cover of observation (left panel) and the differences of ECHAM_CTRL (middle panel) and ECHAM_SMCM (right panel) relative to observation

Figure 2 JJAS-mean shortwave (left panel), longwave (middle panel) and net (right panel) cloud forcing (W m^{-2}) of (a, d, g) observation and the difference between (b, e, h) ECAHM_CTRL and (c, f, i) ECHAM_SMCM and observation (positive is downward).

Figure 3 Same as in Fig.2 but for the shortwave radiation (W m^{-2}; left panel) and outgoing longwave radiation (W m^{-2}; right panel) at the top-of-the-atmosphere

Figure 4 JJAS-mean precipitation (shading; mm day^{-1}) and vertical velocity (contour; Pa s^{-1}) of (a) Observation, (b) ECHAM_CTRL, and (c) ECHAM_SMCM. Negative vertical velocity denotes the upward motion

Figure 5 JJAS mean of the net energy flux into the atmosphere ($\overline{F_{net}}$; upper panel), vertical integral of horizontal moist enthalpy advection ($-\langle\overline{\vec{V}\cdot\nabla M}\rangle$; middle panel), and vertical integral of vertical MSE convection ($-\overline{\langle\omega\,\partial h/\partial p\rangle}$; lower panel) of (a) Observation, (b) ECHAM_CTRL, and (c) ECAHM_SMCM. Units in W m^{-2}.

Figure 6 Area-averaged value of the net energy flux into the atmosphere ($\overline{F_{net}}$), vertical integral of horizontal moist enthalpy advection ($-\langle\overline{\vec{V}\cdot\nabla M}\rangle$), vertical integral of vertical MSE convection ($-\overline{\langle\omega\,\partial h/\partial p\rangle}$), and residual.

Figure 7 JJAS-mean total cloud cover of (a) observation, (b) ECHAM_CTRL, (c) ECHAM_SMCM, the difference between observation and (d) ECHAM_CTRL and (e) ECHAM_SMCM, and (e) the difference between ECHAM_SMCM and ECHAM_CTRL.

Figure 8 JJAS mean of vertical integral of horizontal moist enthalpy advection ($-\overline{\langle \vec{V} \cdot \nabla M \rangle}$; upper panel), horizonal dry enthalpy advection ($-c_p\overline{\langle \vec{V} \cdot \nabla T \rangle}$; middle panel), and latent energy advection ($-l_v\overline{\langle \vec{V} \cdot \nabla q \rangle}$; lower panel) of (a) observation, (b) ECHAM_CTRL, and (c) ECHAM_SMCM. Units in W m^{-2}.

Figure 9 JJAS mean of vertical integral of the (a, d, g) stationary eddy dry enthalpy by the zonal-mean flow $-l_v\overline{[\vec{V}]} \cdot \overline{\nabla q^*}$, (b, e, h) zonal-mean dry enthalpy by the stationary eddy velocity $-l_v\overline{\vec{V}^*} \cdot \overline{[\nabla q]}$, and (c, f, i) pure stationary eddy flux $-l_v\overline{\vec{V}^*} \cdot \overline{\nabla q^*}$ in (left panel) Observation, (middle panel) ECHAM_CTRL, and (right panel) ECHAM_SMCM.

Figure 10 JJAS mean of (a, e, i) Evaporation $\bar{E}$ (contour; CI is 0.25 mm day^{-1}) and the vertical integral of convergence of moist flux $-\overline{\langle \nabla \cdot \vec{V}q \rangle}$ (shading), (b, f, j) vertical convection of moist $-\overline{\langle \partial_p \omega q \rangle}$, (c, g, k) zonal moisture convergence $-\overline{\langle \partial_x (uq) \rangle}$, and (d, h, l) meridional moisture convergence $-\overline{\langle \partial_y (vq) \rangle}$. Unit in mm day^{-1}.

Figure 11 The area-averaged precipitation ($\bar{P}$; PRECIP), evaporation ($\bar{E}$; EVAP), the vertical integral of moist-flux convergence ($-\overline{\langle \nabla \cdot \vec{V}q \rangle}$; -div(Vq)) , vertical convection of moist (-$\overline{\langle \partial_p \omega q \rangle}$; -dp(wq)), zonal moisture convergence ($-\overline{\langle \partial_x (uq) \rangle}$; -dx(uq)), and meridional moisture convergence ($-\overline{\langle \partial_y (vq) \rangle}$; -dy(vq)) over the domain (7°-22°N and 110°-150°E).

Table 1 Area-weighted mean of $-\overline{l_v\langle\vec{V}\cdot\nabla q\rangle}$, $-l_v\langle\left[\vec{\bar{V}}\right]\cdot\overline{\nabla q^*}\rangle$, $-l_v\langle\overline{\vec{V^*}}\cdot\overline{[\nabla q]}\rangle$, $-l_v\langle\overline{\vec{V^*}}\cdot\overline{\nabla q^*}\rangle$, and $-l_v\langle\overline{\vec{V'}\cdot\nabla q'}\rangle$ in the WNP (unit: W m^{-2})

	Observation	ECHAM_CTRL	ECHAM_SMCM
$-\overline{l_v\langle\vec{V}\cdot\nabla q\rangle}$	-11.77	-3.83	-7.69
$-l_v\langle\left[\vec{\bar{V}}\right]\cdot\overline{\nabla q^*}\rangle$	-14.99	-7.43	-13.75
$-l_v\langle\overline{\vec{V^*}}\cdot\overline{[\nabla q]}\rangle$	31.42	12.64	23.71
$-l_v\langle\overline{\vec{V^*}}\cdot\overline{\nabla q^*}\rangle$	-25.50	-10.39	-18.60
$-l_v\langle\overline{\vec{V'}\cdot\nabla q'}\rangle$	-1.56	0.04	-0.44

Table 2 Area-averaged value of $-\overline{\langle \partial_x(uq) \rangle}$, $-\langle \overline{u^*} \times \overline{\partial_x q^*} \rangle$, $-\langle \overline{[u]} \times \overline{\partial_x q^*} \rangle$, $-\langle \overline{[q]} \times \overline{\partial_x u^*} \rangle$, and $-\langle \overline{q^*} \times \overline{\partial_x u^*} \rangle$ in the WNP (unit: mm day^{-1})

	Observation	ECHAM_CTRL	ECHAM_SMCM
$-\overline{\langle \partial_x(uq) \rangle}$	7.72	4.68	7.46
$-\langle \overline{u^*} \times \overline{\partial_x q^*} \rangle$	0.12	0.14	0.14
$-\langle \overline{[u]} \times \overline{\partial_x q^*} \rangle$	-0.40	-0.14	-0.30
$-\langle \overline{[q]} \times \overline{\partial_x u^*} \rangle$	6.93	4.07	6.94
$-\langle \overline{q^*} \times \overline{\partial_x u^*} \rangle$	1.11	0.58	0.82

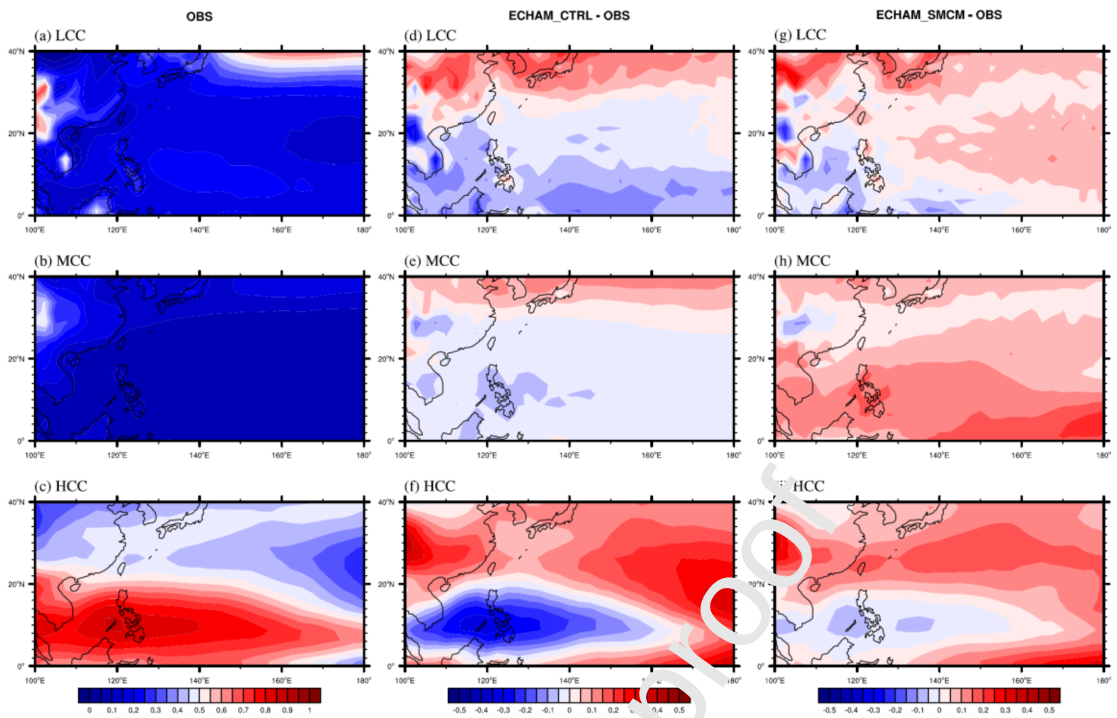

Figure 1 JJAS-mean (a, d, g) low-level, (b, e, h) middle-level, and (c, f, i) high-level cloud cover of observation (left panel) and the differences of ECHAM_CTRL (middle panel) and ECHAM_SMCM (right panel) relative to observation

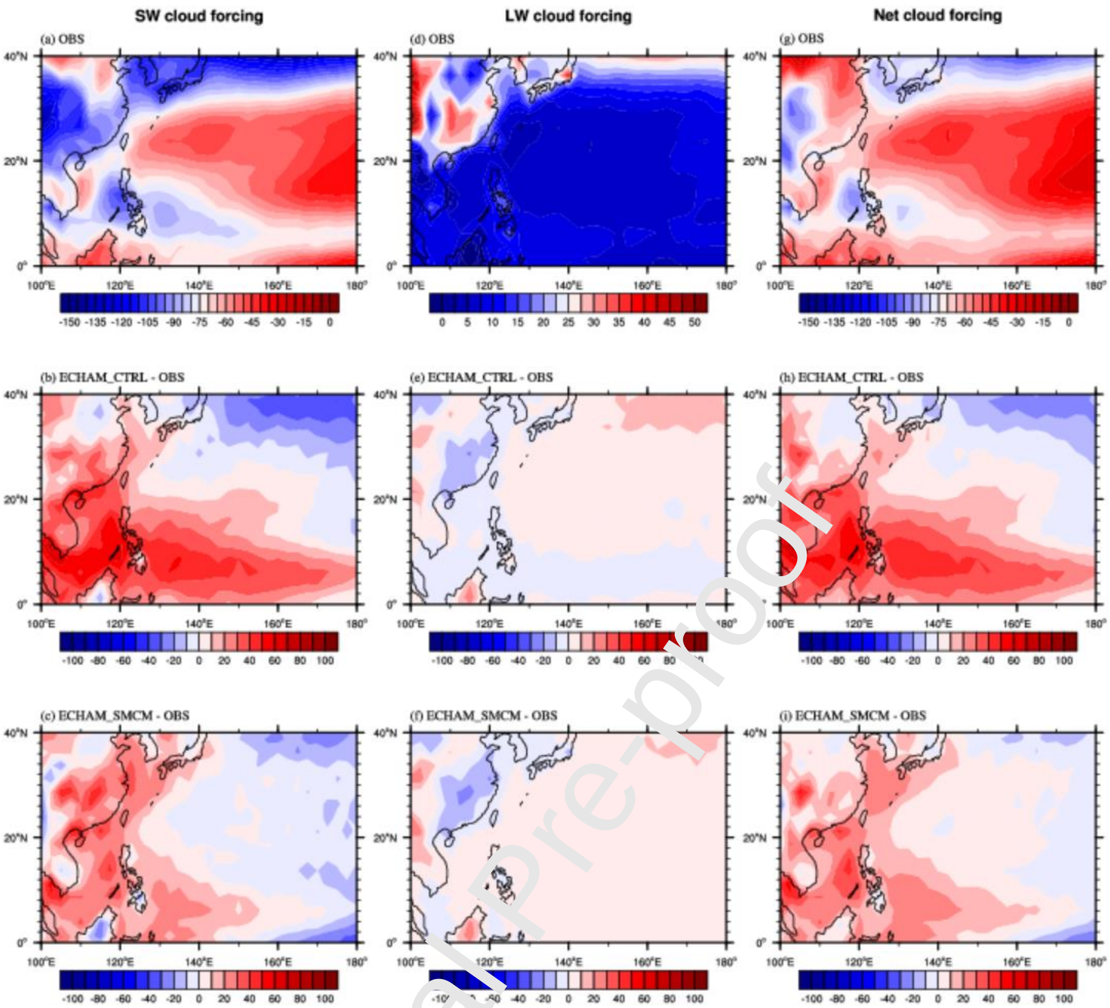

Figure 2 JJAS-mean shortwave (left panel), longwave (middle panel) and net (right panel) cloud forcing (W m^{-2}) of (a, d, g) observation and the difference between (b, e, h) ECAHM_CTRL and (c, f, i) ECHAM_SMCM and observation (positive is downward).

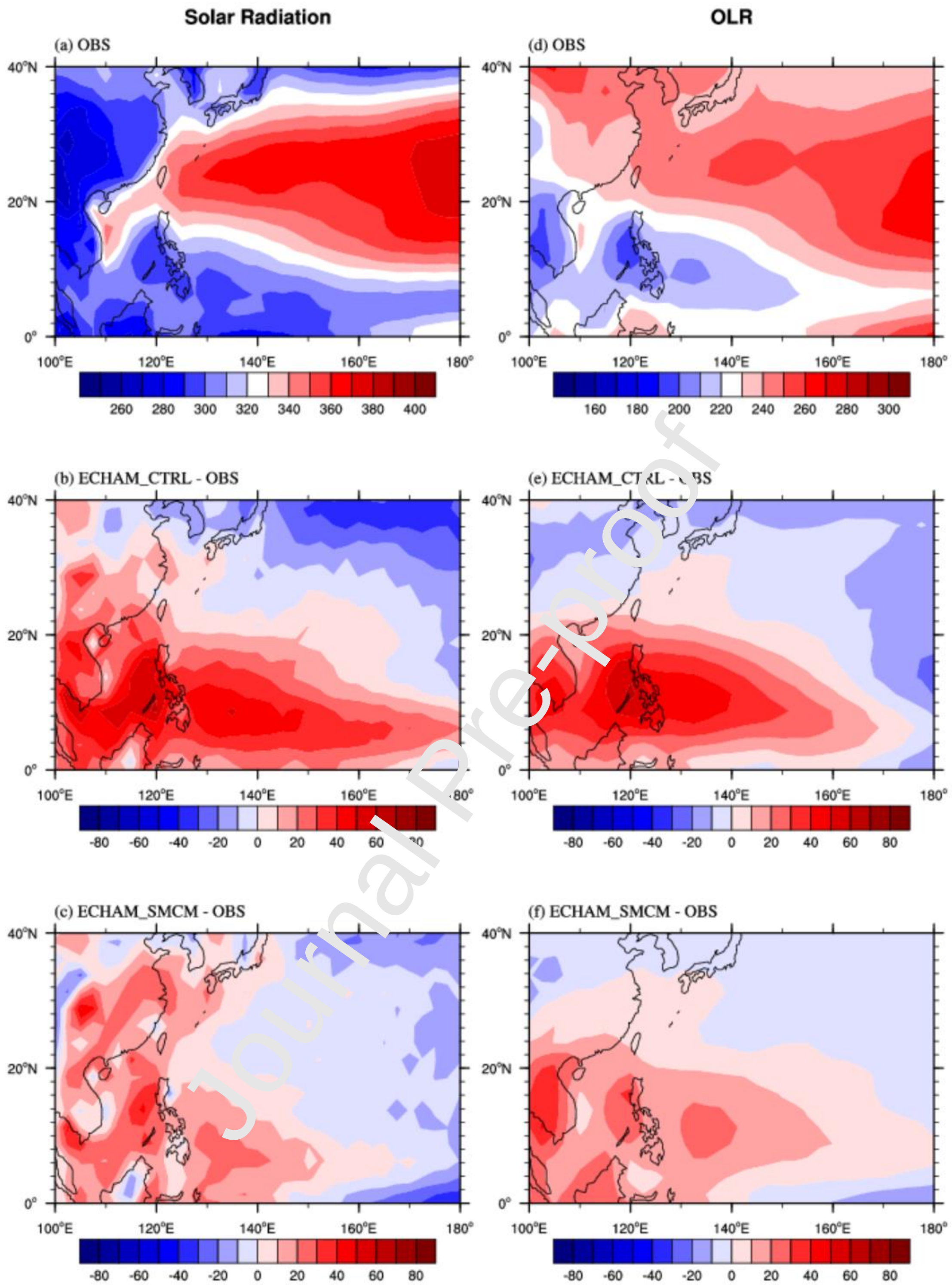

Figure 3 Same as in Fig.2 but for the shortwave radiation (W m^{-2}; left panel) and outgoing longwave radiation (W m^{-2}; right panel) at the top-of-the-atmosphere.

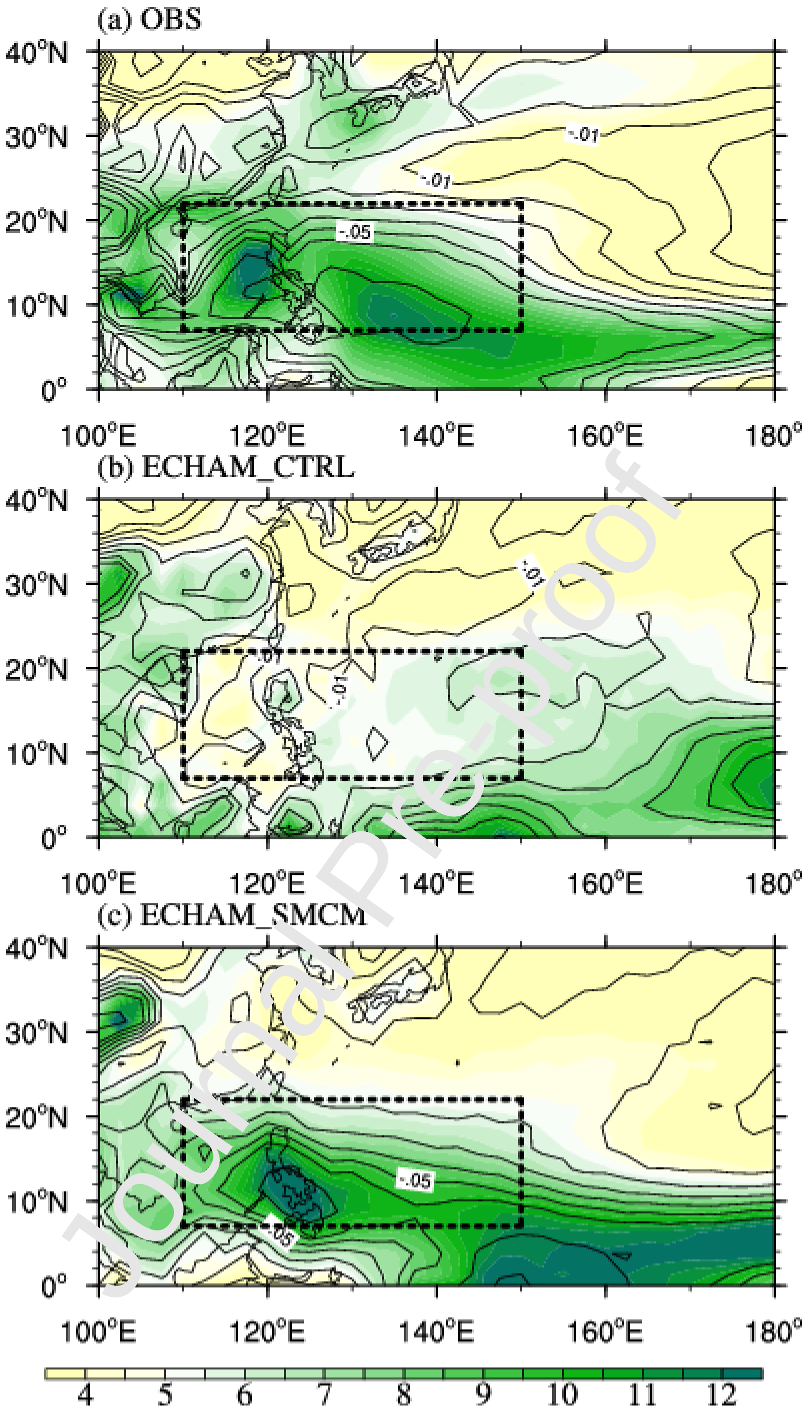

Fig. 4 JJAS-mean precipitation (shading; mm day^{-1}) and vertical velocity (contour; Pa s^{-1}) of (a) Observation, (b) ECHAM_CTRL, and (c) ECHAM_SMCM. Negative vertical velocity denotes the upward motion

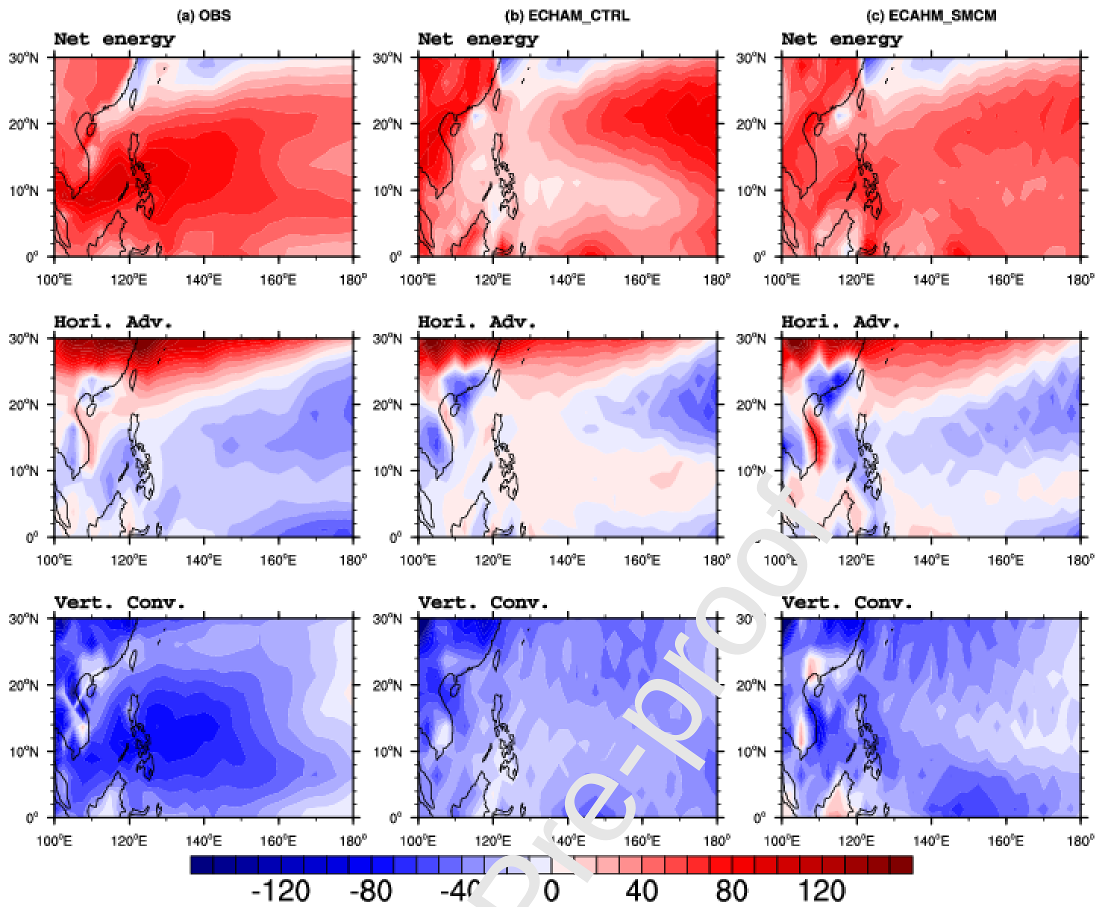

Fig. 5 JJAS mean of the net energy flux into the atmosphere ($\overline{F_{net}}$; upper panel), vertical integral of horizontal moist enthalpy advection ($-\overline{\langle\vec{V}\cdot\nabla M\rangle}$; middle panel), and vertical integral of vertical MSE convection ($-\overline{\langle\omega\,\partial h/\partial p\rangle}$; lower panel) of (a) Observation, (b) ECHAM_CTRL, and (c) ECAHM_SMCM. Unit is W m^{-2}

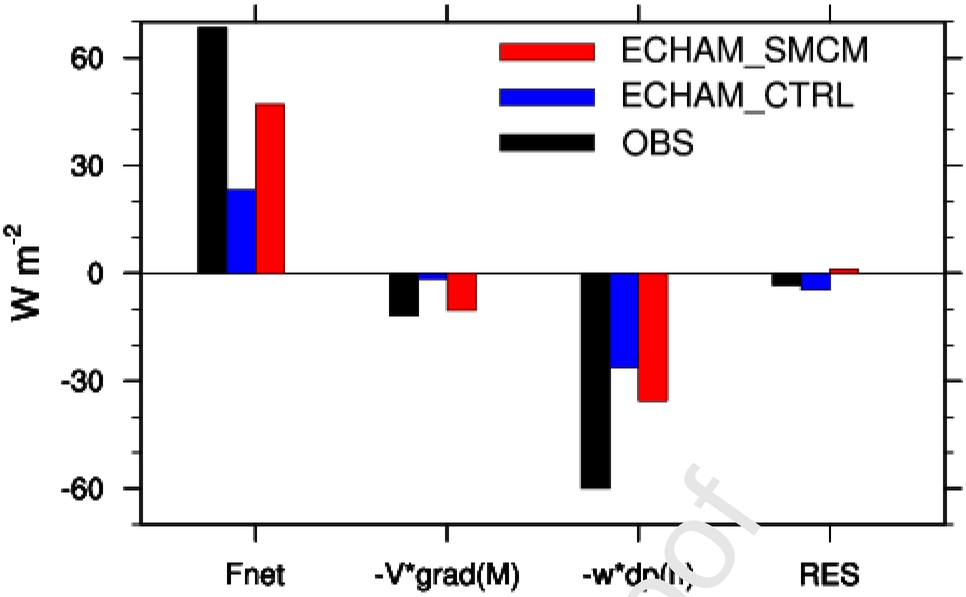

Fig. 6 Area-averaged value of the net energy flux into the atmosphere ($\overline{F_{net}}$), vertical integral of horizontal moist enthalpy advection ($-\overline{\langle\vec{V}\cdot\nabla M\rangle}$), vertical integral of horizontal moist static energy convection ($-\overline{\langle\omega\,\partial h/\partial p\rangle}$), and residual

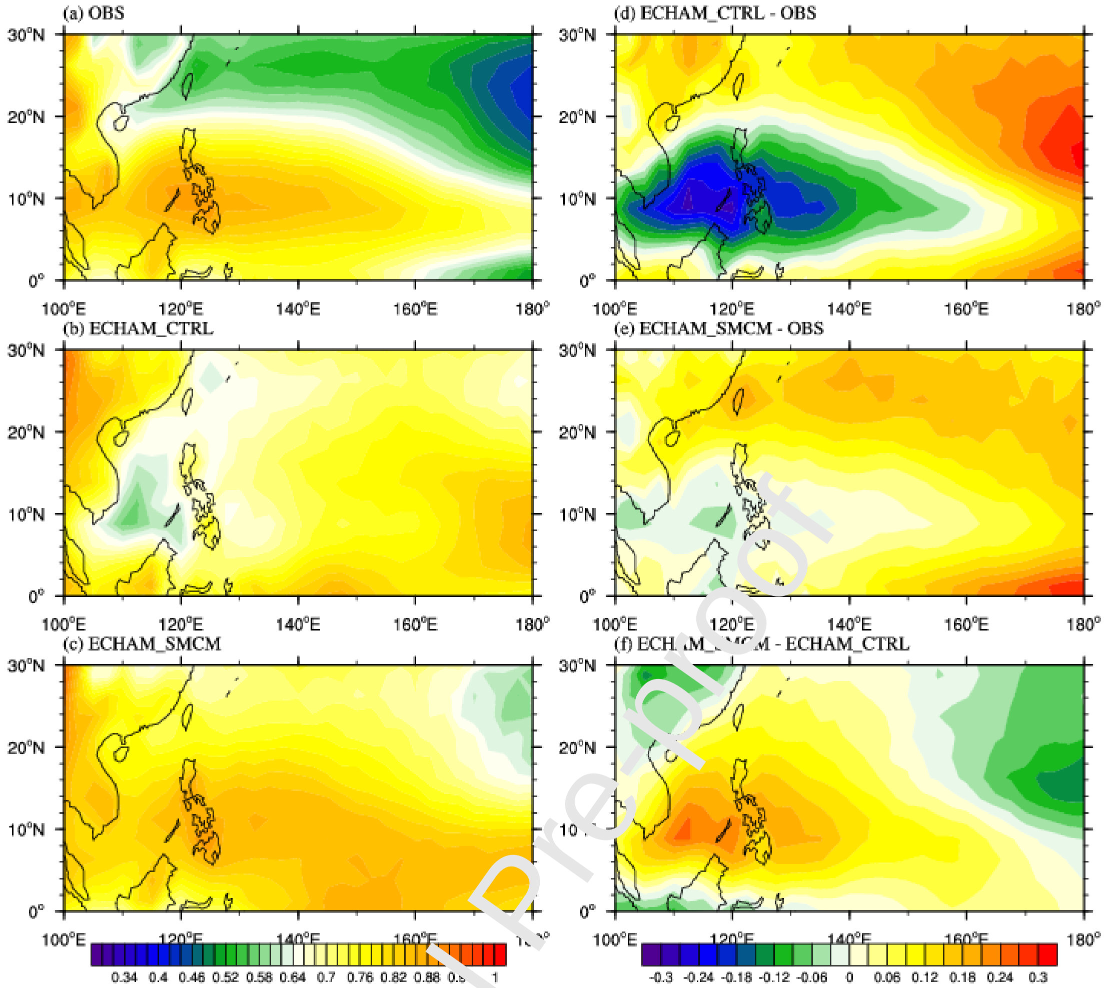

Fig. 7 JJAS-mean total cloud cover of (a) observation, (b) ECHAM_CTRL, (c) ECHAM_SMCM, the difference between observation and (d) ECHAM_CTRL and (e) ECHAM_SMCM, and (f) the difference between ECHAM_SMCM and ECHAM_CTRL

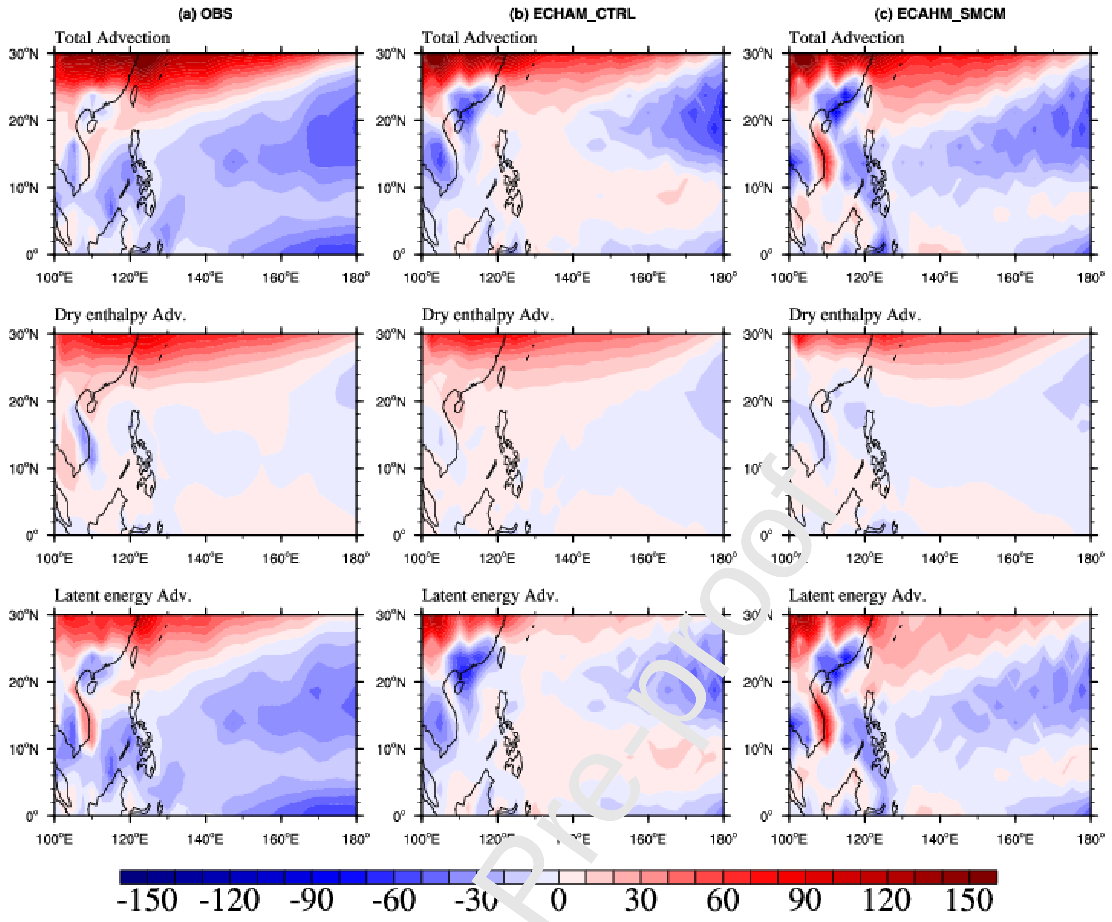

Fig. 8 JJAS mean of vertical integral of horizontal moist enthalpy advection ($-\overline{\langle\vec{V}\cdot\nabla M\rangle}$; upper panel), horizontal dry enthalpy advection ($-\overline{c_p\langle\vec{V}\cdot\nabla T\rangle}$; middle panel), and latent energy advection ($-\overline{l_v\langle\vec{V}\cdot\nabla q\rangle}$; lower panel) of (a) observation, (b) ECHAM_CTRL, and (c) ECHAM_SMCM. Unit is W m^{-2}

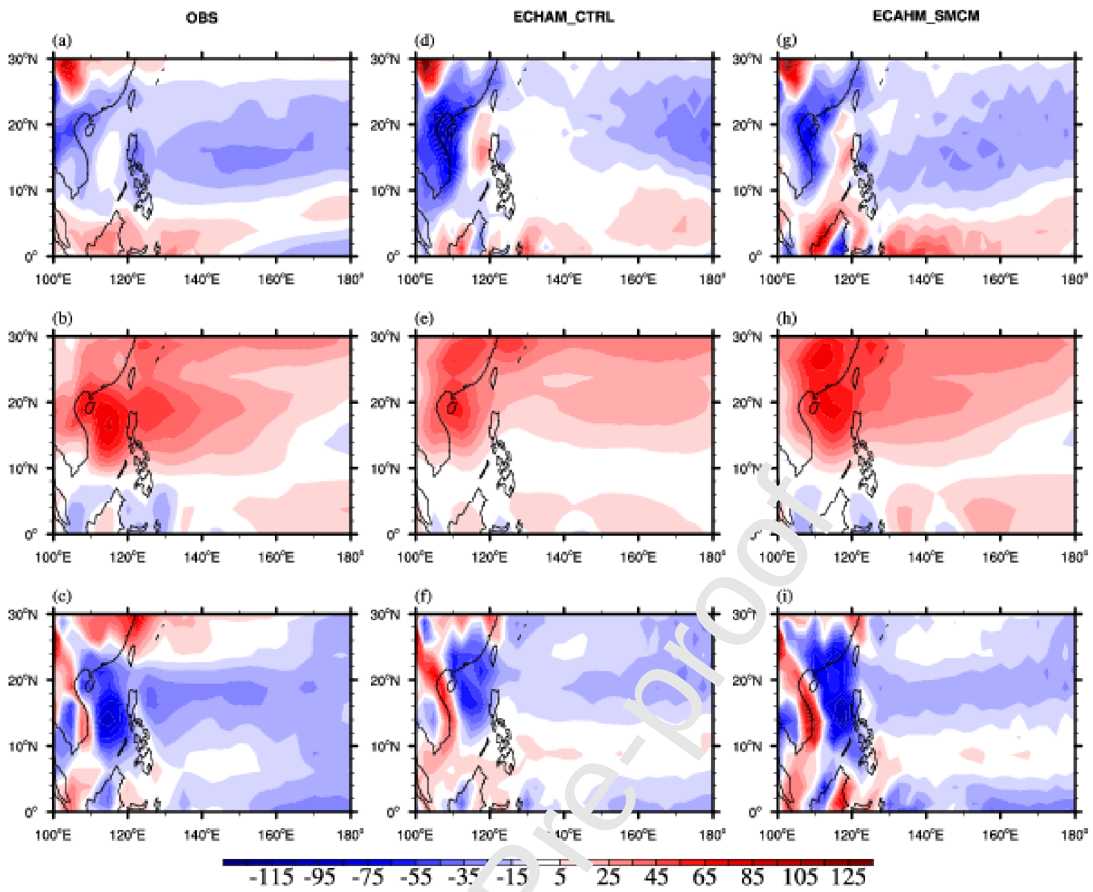

Fig. 9 JJAS mean of vertical integral of the (a, d, g) stationary eddy dry enthalpy by the zonal-mean flow $-l_v\overline{[\vec{V}]}\cdot\overline{\nabla q^*}$, (b, e, h) zonal-mean dry enthalpy by the stationary eddy velocity $-l_v\overline{\vec{V}^*}\cdot\overline{[\nabla q]}$ and (c, f, i) pure stationary eddy flux $-l_v\overline{\vec{V}^*}\cdot\overline{\nabla q^*}$ in Observation(left panel), ECHAM_CTRL(middle panel), and ECHAM_SMCM (right panel)

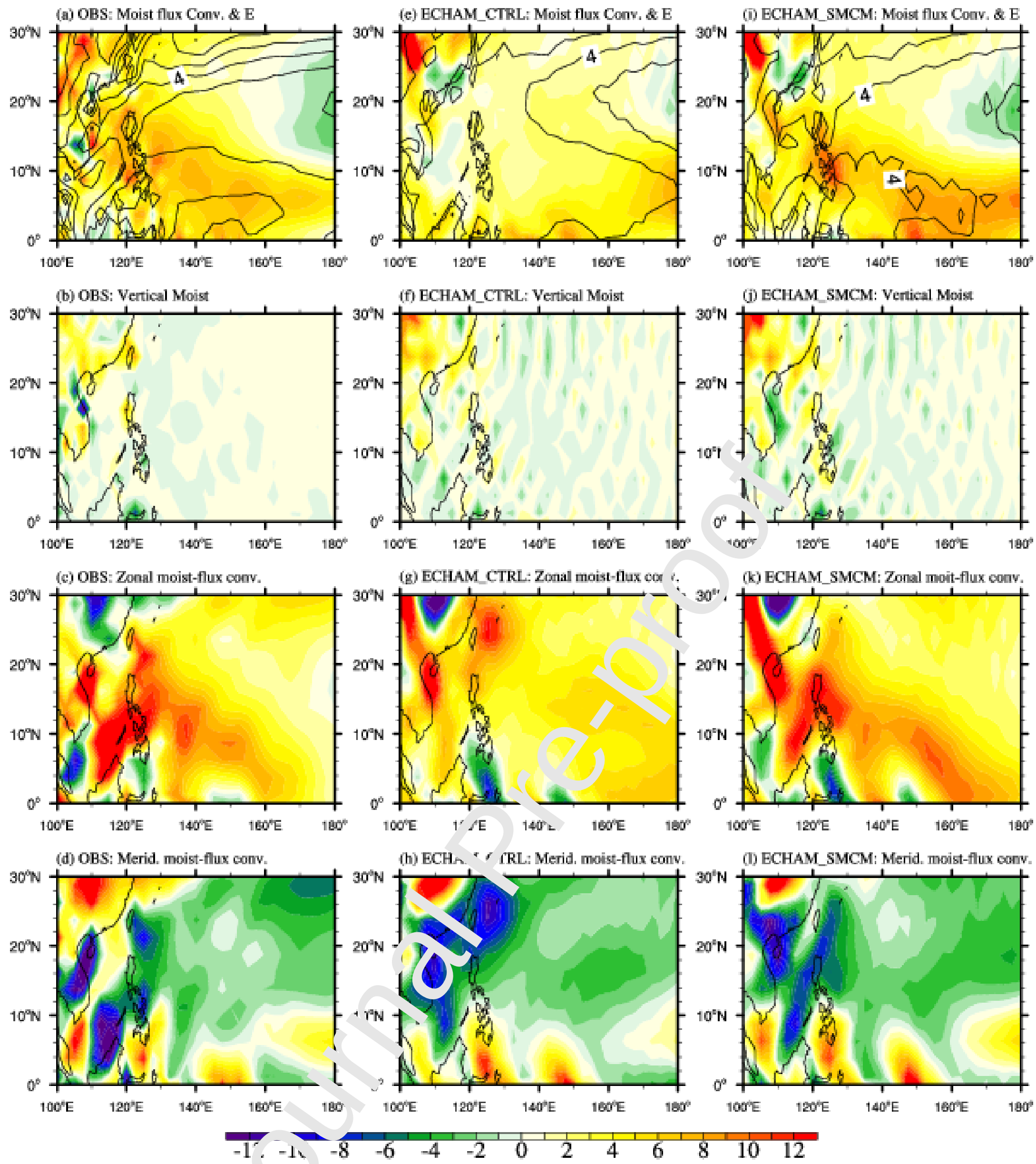

Fig. 10 JJAS mean of (a, e, i) Evaporation $\bar{E}$ (contour; CI is 0.25 mm day^{-1}) and the vertical integral of convergence of moist flux $-\overline{\langle \nabla \cdot \vec{V} q \rangle}$ (shading), (b, f, j) vertical convection of moist $-\overline{\langle \partial_p \omega q \rangle}$, (c, g, k) zonal moisture convergence $-\overline{\langle \partial_x (uq) \rangle}$, and (d, h, l) meridional moisture convergence $-\overline{\langle \partial_y (vq) \rangle}$. Unit is mm day^{-1}

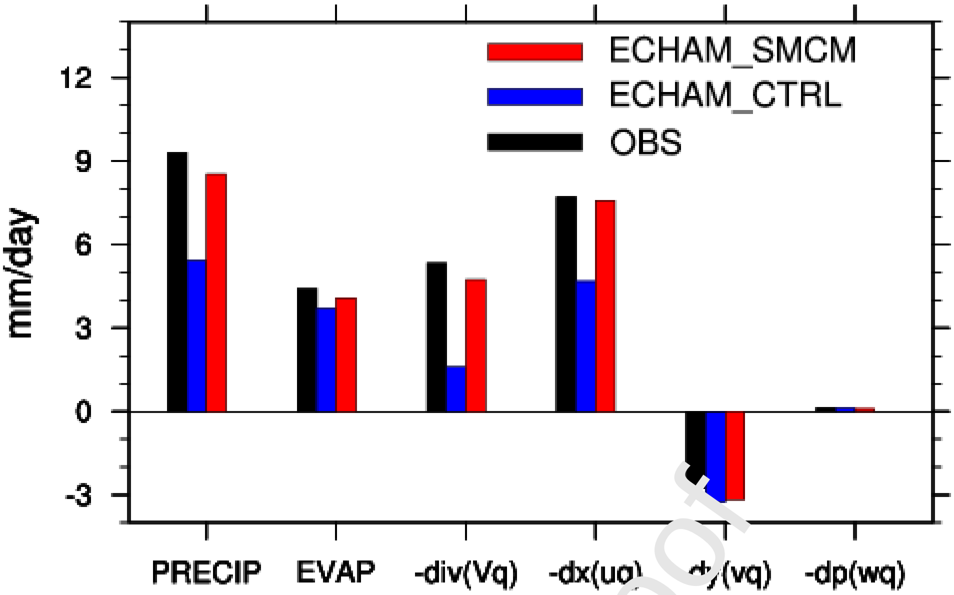

Fig. 11 The area-averaged precipitation ($\bar{P}$; PRECIP), evaporation ($\bar{E}$; EVAP), the vertical integral of moist-flux convergence ($-\overline{\langle\nabla \cdot \vec{V}q\rangle}$; -div(Vq)) , vertical convection of moist ($-\overline{\langle\partial_p \omega q\rangle}$; -dp(wq)), zonal moisture convergence ($-\overline{\langle\partial_x (uq)\rangle}$; -dx(uq)), and meridional moisture convergence ($-\overline{\langle\partial_y (vq)\rangle}$; -dy(vq)) over the domain (7º-22ºN and 110º-150ºE)

Author Statement

Manuscript title: Impacts of the Stochastic Multicloud Parameterization on the Simulation of Western North Pacific Summer Rainfall

Libin Ma: Design, analysis, and interpretation of data for the work; AND drafted the work and revised it critically for important intellectual content; AND approved the final version to be published.

Shuangyan Yang: Interpretation of data for the work; AND revised the work critically for important intellectual content.

Declaration of interests

☒ The authors declare that they have no known competing financial interests or personal relationships that could have appeared to influence the work reported in this paper.

☐The authors declare the following financial interests/personal relationships which may be considered as potential competing interests:

1. Cloud cover and radiation over the western North Pacific in boreal summer are improved via incorporating the Stochastic Multicloud Model (SMCM) into ECHAM6.3;

2. Simulation of the western North Pacific summer precipitation is improved by coupling the SMCM into ECHAM6.3.